Article

Preparation of TiSi$_2$ Powders with Enhanced Lithium-Ion Storage via Chemical Oven Self-Propagating High-Temperature Synthesis

Jianguang Xu *, Menglan Jin, Xinlu Shi, Qiuyu Li, Chengqiang Gan and Wei Yao *

School of Materials Science and Engineering, Yancheng Institute of Technology, Yancheng 224051, China; Jinml1234567@163.com (M.J.); Shixinlu1998@163.com (X.S.); liqiuyu945@163.com (Q.L.); 15905103523@163.com (C.G.)
* Correspondence: jgxu@163.com (J.X.); xiaoniu1981@126.com (W.Y.)

Abstract: Although silicon has highest specific capacity as anode for lithium-ion battery (LIB), its large volume change during the charge/discharge process becomes a great inevitable hindrance before commercialization. Metal silicides may be an alternative choice because they have the ability to accommodate the volume change by dispersing Si in the metal matrix as well as very good electrical conductivity. Herein we report on the suitability of lithium-ion uptake in C54 TiSi$_2$ prepared by the "chemical oven" self-propagating high-temperature synthesis from the element reactants, which was known as an inactive metal silicide in lithium-ion storage previously. After being wrapped by graphene, the agglomeration of TiSi$_2$ particles has been efficiently prevented, resulting in an enhanced lithium-ion storage performance when using as an anode for LIB. The as-received TiSi$_2$/RGO hybrid exhibits considerable activities in the reversible lithiation and delithiation process, showing a high reversible capacity of 358 mAh/g at a current density of 50 mA/g. Specially, both TiSi$_2$ and TiSi$_2$/RGO electrodes show a remarkable enhanced electrochemical performance along with the cycle number, indicating the promising potential in lithium-ion storage of this silicide. Ex-situ XRD during charge/discharge process reveals alloying reaction may contribute to the capacity of TiSi$_2$. This work suggests that TiSi$_2$ and other inactive transition metal silicides are potential promising anode materials for Li-ion battery and capacitor.

Keywords: TiSi$_2$; self-propagating high-temperature synthesis; electrochemical performance; lithium-ion battery

1. Introduction

The fast development of portable electrical equipment and electric vehicle creates a daunting demand for energy storage devices with high energy and power densities [1]. As a key unit for energy storage, lithium-ion batteries are experiencing a revolutionary tendency to reach the target of lightweight, long lifetime and good cycleability. In considering the low capacity (372 mAh/g) of commercial carbon anode, great efforts have been done to find some novel anode materials with high capacity. Due to the extremely high theoretical capacity (4200 mAh/g), silicon becomes one of the most attractive anode materials for lithium-ion battery [2–4]. However, it sustains from its low intrinsic electric conductivity and large structural volume changes during charge/discharge cycling [5]. This gives rise to serious mechanical stresses that consequently results in the pulverization of the active mass particles, eventually inevitable capacity fade [6–8].

As an attempt to overcome the drawbacks of silicon, metal silicides, which have good electric conductivity, were first investigated by Anani and Huggins as anodes for lithium-ion battery [9]. Since then, more researches have been done to evaluate the electrochemical behavior of metal silicides [10,11]. For example, the specific capacity of Mg$_2$Si with an anti-fluorine structure is as high as ~400 mAh/g [12,13], and after being coated with carbon, the

capacity of C@Mg$_2$Si further reached 726 mAh/g [14]. The CrSi$_2$ and MoSi$_2$ synthesized by high energy ball milling show a reversible capacity of 340 and 130 mAh/g after 20 cycles at C/12, respectively, which is much higher than the commercial counterparts [15]. In the case of TiSi$_2$, although the ordinary C54 type was reported as an inactive anode material for LIB [16], the C49 type nanonet shows excellent electrochemical performance as an anode, the reversible specific capacity of which is greater than 500 mAh/g [17]. Unfortunately, the application of this TiSi$_2$ nanonet may hindered by the high cost of CVD method using SiH$_4$ and TiCl$_4$ as raw materials. Compared to the metastable C49 TiSi$_2$, the C54 TiSi$_2$ is thermodynamic stable and easier to be mass produced via cost effective method. In addition, if C54 TiSi$_2$ could be transformed to low silicon silicides such as TiSi or Ti$_5$Si$_3$ during lithiation, it will exhibit high lithium-ion storage potential.

Thus, considering the low cost and remarkable potential in lithium-ion storage, we decided to explore the electrochemical performance of C54 TiSi$_2$ as an anode for LIB. TiSi$_2$ has been found to have broad applications as a thin film in microelectronics due to its remarkably high electrical conductivity, high temperature stability, and excellent mechanical property and corrosion resistance [18–20]. In addition, TiSi$_2$ improved the battery behavior of Si-based anode materials significantly through increasing the electrical conductivity when it has been added to Si-based anode [21–23]. Specially, the TiSi$_2$-air system exhibits very high energy density, which is more than 3–10 times higher than that of zinc-air or aluminum-air systems [24]. However, although Anani and Huggins predicted that TiSi is a potential anode material for LIB [9], the bulk C54 TiSi$_2$ shows negligible capacity as we discussed above [16]. Fortunately, it has been well accepted that, the nanosized materials will show enhanced properties with respect to their corresponding bulk counterpart [25–27]. The reversible capacity of TiSi$_2$ nanowire is better than the bulk one, although its value is still very low (65 mAh/g) [17]. On the other hand, designing special structure, including doping, making defects and adding carbon, is considered as an alternate effective way for optimizing the activity of the electrode. For example, The specific capacity of graphene was detected to be 540 mAh/g [28], while that of nitrogen-doped graphene achieved 684 mAh/g [29], and the flash reduced graphene with many defects have the ability of tolerating high current rate (156 mAh/g at 40C) [30]. The capacity of the interconnected porous silicon/carbon hybrids is kept at 1036.6 mAh/g after 100 cycles at 50 mA/g [31], and the graphene/Si–C hybrid anode shows high areal capacity (3.2 mAh/cm^2 after 100 cycles at 50 mA/g) for LIB due to its dual conductive network [32].

In this work, pure TiSi$_2$ was synthesized by the "chemical-oven" self-propagating high-temperature synthesis (COSHS). The merits of SHS lie on the fast reaction, energy-saving, and the ability to form very fine particles with many defects if considering high-temperature deformation and fast transformation [33,34]. Then, reduced graphene oxide (RGO) was used to wrap up the TiSi$_2$ particles for constructing a homogeneous hybrid with high conductive network. The battery performance of the TiSi$_2$ and TiSi$_2$/RGO anodes were investigated in detail.

2. Materials and Methods

2.1. Synthesis of TiSi$_2$

99% pure titanium powder with an average particle size of 35 μm, and 99% pure Si powder with an average particle size of 65 μm were used in this work. The mixture of Si and Ti (atomic ratio 2:1) was immersed in ethanol in a steel container and then ball milled using agate balls at a speed of 300 rpm for 3 h. The resulting slurry was dried in a drying cabinet at 80 °C for 5 h. The dried powder was then sieved to 100 mesh and collected for the following "chemical oven" self-propagating high-temperature synthesis (COSHS) procedure. The Ti + 2Si mixture was placed inside a graphite crucible, while the Ti + C mixture, used as a chemical furnace, was placed outside. Carbon is present between the inside and outside. The two mixtures are in contact with each other at the bottom of the graphite crucible. Then, the powders were burned via electrifying tungsten placed

in the upper surface of the outer powders in a steel chamber at a pressure of 0.2 MPa Ar (99.9 wt.%). The synthesized powder was collected and ball milled at a speed of 300 rpm for 3 h to perform the following operations.

In order to remove impurities in the synthesized $TiSi_2$ powder, 3 g of $TiSi_2$ powder was dispersed in 100 mL of 2 M NaOH aqueous solution and stirred vigorously for 24 h. Then the purified $TiSi_2$ was collected via washing the mixture in deionized water and vacuum drying.

2.2. Synthesis of Graphite Oxide

Graphite oxide (GO) was synthesized by a modified Hummers method. Generally, a mixture of 3 g graphite, 2.5 g P_2O_5, 2.5 g $K_2S_2O_8$ and 12 mL concentrated H_2SO_4 was stirring for 6 h in a flask at 80 °C. After cooling, it was diluted carefully with deionized water, then filtered and washed on the filter until the pH value of the washed water became neutral. After drying at the ambient temperature, the obtained pre-oxidized graphite powder was dispersed in 120 mL of concentrated H_2SO_4 in an ice bath. Then, 30 g of $KMnO_4$ was added to the dispersion gradually with stirring. After that, the mixture was stirred at 35 °C for 2 h, and then 200 mL of deionized water was added dropwise. The dispersion was then stirred for another 30 min, and the reaction was stopped by adding 0.5 L of deionized water and 20 mL of 30% H_2O_2, after which the color of the dispersion changed to bright yellow. The dispersion was filtered and washed with 1 M HCl aqueous solution to remove metal ions. For further purification, graphitate oxide was dialyzed weekly to remove residual salts and acids. The concentration of the resulting solution was ~7 mg/g.

2.3. Preparation of TiSi$_2$/Graphene (RGO) Hybrid Material

The hybrid material was synthesized based on a simple one-pot method. Usually, 3.05 g of graphite oxide solution was dispersed in 100 mL of deionized water and ultrasonically treated for 1 h, and then left to stand in a magnetic stirrer for 6 h to produce GO solution. After that, 0.103 g of purified $TiSi_2$ powder was added to the solution, followed by ultrasonic treatment for 1 h and stirring for 6 h. Then, 30 μL of 80% hydrazine was added to the mixed solution and stirred in a water bath at 30 °C for 12 h. Finally, the precipitate was gathered via centrifugation and washing with ethanol and deionized water.

2.4. Preparation of Electrodes

The CR-2032 coin cells using lithium metal film as the counter electrode and reference electrode were used to evaluate the electrochemical performance of $TiSi_2$ particles and $TiSi_2$/graphene hybrid particles. The battery is based on lithium metal $(-)$ | electrolyte | $TiSi_2$ or $TiSi_2$/RGO hybrid $(+)$, and the electrolyte is 1 M $LiPF_6$ in ethylene carbonate (EC)-dimethyl carbonate (DMC)-methyl ethyl carbonate (EMC) solution (volumetric ratio 1:1:1). A microporous polypropylene film (Celgard 2400, Shanghai, China) was used as the separator. 80 wt.% $TiSi_2$ or $TiSi_2$/RGO with 10 wt.% acetylene black and 10 wt.% polyvinylidene fluoride (PVDF) binder were mixed uniformly in N-methyl pyrrolidinone (NMP), resulting into a viscous slurry for effective deposition. To prepare electrode, the as-received slurry was deposited on a copper foil (10 μm) current collector and dried in a vacuum oven at 100 °C for 12 h. The mass loading of active material is 0.65–0.85 mg/cm^2. Cell assembly was conducted in a glove box filled with pure argon.

2.5. Material Characterization

The morphologies of $TiSi_2$ and $TiSi_2$/RGO hybrid were investigated by a scanning electron microscope. The phase structure was determined by X-ray diffraction analysis of Cu-Kα radiation (λ = 1.5418 Å) at room temperature in the 2θ range of 20° to 70°. FT-IR spectroscopy was performed with a NEXUS-670 Fourier Transform Infrared Spectrometer (Ramsey, MN, USA). The surface area and pore size distribution were measured on a TriStar II 3020 (Norcross, GA, USA) surface area and porosity analysis instrument.

The cells were galvanostatically charged and discharged within a constant voltage range of 0.001 to 3 V on the Shenzhen Neware battery cycler (Shenzhen, China) at room temperature. All gravimetric capacity corresponding to the prepared electrodes were calculated based on the mass of $TiSi_2$ or $TiSi_2/RGO$ hybrid. The electrochemical workstation (Zahner-Zennium, Kronach, Germany) was used for cyclic voltammetry and electrochemical impedance spectroscopy (EIS, frequency range: $0.001–10^5$ Hz, amplitude: 5 mV) analysis. In this work, unless otherwise specified, all impedance measurements were performed after three cycles of the prepared electrodes.

3. Results and Discussion

The XRD pattern of the combustion product (unpurified $TiSi_2$) shows that $TiSi_2$ was successfully synthesized by the chemical oven SHS method. There are no other titanium silicides phases except $TiSi_2$ detected based on the XRD result. Because $TiSi_2$ is the first phase generated in the formation sequence among all the possible titanium silicides [35], when using Ti + 2Si mixture as raw material, $TiSi_2$ is the only reaction product. Besides the main phase $TiSi_2$, residual Si is also detected. It can be observed from the XRD pattern of purified $TiSi_2$ that the residual Si was thoroughly removed after treating the product in NaOH aqueous solution. Figure 1a also exhibits the XRD pattern of $TiSi_2/RGO$ hybrid, indicating the crystal structure of $TiSi_2$ has no change after hybridizing purified $TiSi_2$ with RGO.
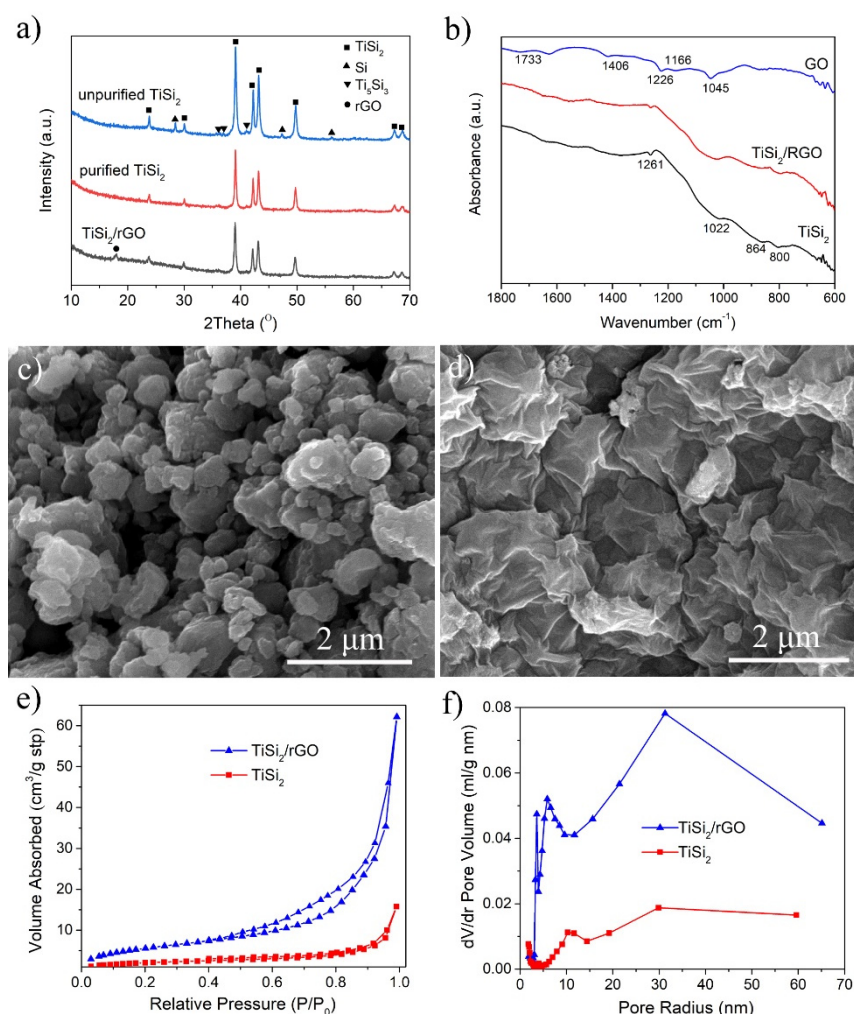

Figure 1. (**a**) XRD patterns of $TiSi_2$, purified $TiSi_2$ and $TiSi_2/RGO$; (**b**) FT-IR spectra of graphene oxide (GO), $TiSi_2$ and $TiSi_2/RGO$; SEM micrographs of (**c**) $TiSi_2$ and (**d**) $TiSi_2/RGO$; (**e**) N$_2$ adsorption-desorption isotherms and (**f**) pore size distributions of $TiSi_2$ and $TiSi_2/rGO$.

Meanwhile the $TiSi_2$/RGO hybrid is further proved by FT-IR spectra. Figure 1b shows the FT-IR spectra of graphene oxide (GO), $TiSi_2$, and $TiSi_2$/RGO hybrid. As shown in Figure 1b, the pattern of GO exhibits a few peaks because there are some oxygen functional groups on its surface. The peak at 1733 cm^{-1} is related to the stretching vibration of –C=O/–COOH. The peaks at 1406 and 1226 cm^{-1} are corresponding to the stretching vibration of O-H and C–OH in tertiary alcohol, respectively, and those at 1166 and 1045 cm^{-1} are associated with the absorption of C–O [36]. These peaks disappeared when the GO has been reduced, thus they cannot be detected in the pattern of $TiSi_2$/RGO hybrid. In addition, the FT-IR spectra of $TiSi_2$ and $TiSi_2$/RGO are similar, indicating the $TiSi_2$/RGO was successfully obtained in this work and $TiSi_2$ did not change during the reduction process. It can be also concluded from the FT-IR spectra that $TiSi_2$ particles are coated by a thin oxide film, because the weak peaks at 1264, 1022, and 800 cm^{-1} can be attributed to Si–O–Si bond, while the peak at 864 cm^{-1} is corresponding to Si–O–Ti bond [37].

Figure 1c,d shows SEM micrographs of $TiSi_2$ and the $TiSi_2$/RGO hybrid. The as-synthesized $TiSi_2$ particles range from approximately 0.3 μm to 2 μm, and each particle consists of many small primary particles. This aggregation of $TiSi_2$ primary particles will prevent the diffusion of Li ion, resulting in a limited electrochemical performance. In this consideration, sonication was applied to avoid the agglomeration during hybridizing $TiSi_2$ with graphene. As a result, separated $TiSi_2$ particles have been warped up tightly by folded RGO nanosheets which were in situ reduced by hydrazine in the graphene oxide/$TiSi_2$ hybrid dispersion, showing a good distribution in RGO nanosheets. In addition, RGO nanosheets contacted well with each other, resulting in a fast electron conductive network when using as an electrode for LIB.

The exposed surface area and pore size distributions of $TiSi_2$ and $TiSi_2$/RGO hybrid were further investigated by N_2 absorption/desorption tests, shown Figure 1e,f. A typical type-IV isotherm curve of $TiSi_2$/RGO with an obvious hysteresis loop of type H3 can be observed in Figure 1e, indicating the incorporation of $TiSi_2$ particles between RGO nanosheets giving rise to slit-shaped pores. In addition, the surface area of $TiSi_2$/RGO is 21.33 m^2/g, increased by 205.6% compared to that of pure $TiSi_2$. The increased surface area suggested that adding RGO nanosheets can effectively inhibit the aggregation and the in-situ hybridization of RGO nanosheets. Moreover, as shown in Figure 1f, the $TiSi_2$/RGO hybrid possesses more pores than pure $TiSi_2$. These results obtained by BET method confirmed the porous structure of $TiSi_2$/RGO hybrid, which can supply channels for electrolyte transport and Li^+ ions diffusion, leading to a better electrochemical performance.

Then, $TiSi_2$ and $TiSi_2$/RGO were investigated as anodes for LIBs. Figure 2a,b shows the first three charge-discharge profiles of the $TiSi_2$ and $TiSi_2$/RGO samples in the voltage range of 0.001 to 3 V at a current density of 50 mA/g. The initial charge and discharge capacities of $TiSi_2$ electrode are 184 mAh/g and 95 mAh/g, respectively, and the relevant coulombic efficiency is 51.5%. However, for the graphene-modified $TiSi_2$ anode, these specific capacities are increased to 478 mAh/g and 378 mAh/g, respectively, and the relevant coulombic efficiency is as high as 78.8%. Figure 2c,d shows the first two voltammograms (CVs) of $TiSi_2$ and $TiSi_2$/RGO hybrid at a scan rate of 0.1 mV/s. In the 1st cathodic sweep, a peak at around 2.1 V in both anodes' curves can be observed, corresponding to irreversible electrochemical reactions between surface silicon oxide and Li ion [38]. The broad peaks at 0.5–1.5 V for $TiSi_2$ and 0.5–1.1 V for the hybrid can be assigned to the formation of SEI layer on $TiSi_2$ particles. These peaks are unobserved during the following cycles. Then, a sharp peak close to 0 V appeared in both $TiSi_2$ and the hybrid's curves, which can be assigned to the formation of Li_xSi [10,21,39]. Two consecutive anodic peaks can be discovered at 1.2 V and 2.0 V, which are probably the decomposition of Li_xSi and formation of $TiSi_2$. These peaks of the hybrid are still obvious in the second anodic sweep, while those of $TiSi_2$ are very weak, indicating the electrochemical reactions in the hybrid are kept active during following charge/discharge cycles. Thus the hybrid exhibits better electrochemical performance compared to pure $TiSi_2$.
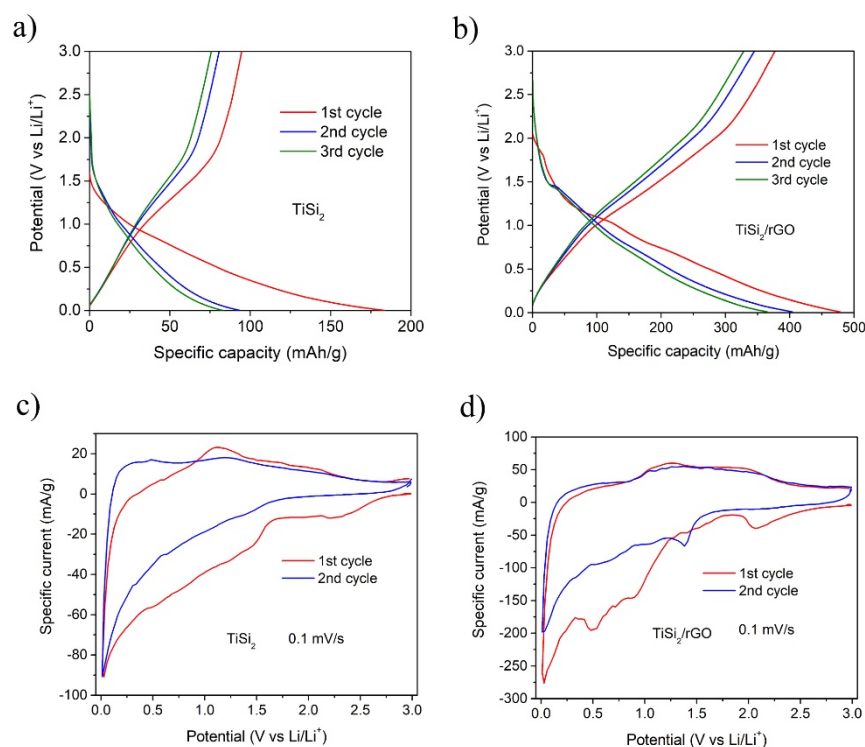
Figure 2. The first three voltage profiles at 50mA/g of (**a**) TiSi$_2$ and (**b**) TiSi$_2$/RGO; CV scans at 0.1 mV/s of (**c**) TiSi$_2$ and (**d**) TiSi$_2$/RGO.

Figure 3a shows the rate behavior of TiSi$_2$ and TiSi$_2$/RGO. When using TiSi$_2$/RGO as an anode, a reversible capacity of 320 mAh/g has been achieved at a current density of 50 mA/g. When the current densities were increased to 100, 200, 400, 1000 and 2000 mA/g, the TiSi$_2$/RGO anode delivered reversible capacities of 314, 296, 265, 214, and 174 mAh/g, respectively. Furthermore, when the current density was reverted to 50 mA/g, the TiSi$_2$/RGO anode recovered a higher capacity of ~358 mAh/g, which is a ~112% of the initial specific capacity, exhibiting an excellent rate performance. However, the TiSi$_2$ electrode has poor rate performance.

Figure 3b shows the cyclic performance of TiSi$_2$ and TiSi$_2$/RGO at a current density of 400 mA/g. The 1st discharge capacity of TiSi$_2$/RGO is 194 mAh/g, while the 2nd discharge capacity is reduced to 171 mAh/g. Particularly, after a few initial cycles, the specific capacity started to gradually increase with cycles and a high specific capacity of 263 mAh/g has been reached after 600 charge-discharge cycles. Moreover, this value still fits a growing trend. The 1st coulombic efficiency is 65%, then it quickly increased to ~100% in a few cycles and maintained stable in following cycles. This lithium ions storage improvement with cycling can be attributed to the continuous activation of TiSi$_2$ by repeated insertion of Li$^+$, leading to much more electrochemically active sites for Li$^+$ insertion or alloying. On the other hand, the pure TiSi$_2$ anode only obtained a low specific capacity of 77 mAh/g after 600 charge-discharge cycles, which is much lower than the TiSi$_2$/RGO anode. The low capacity of pure TiSi$_2$ anode can be ascribed to the agglomeration of primary TiSi$_2$ particles, preventing the electrolyte access and insertion of Li$^+$.
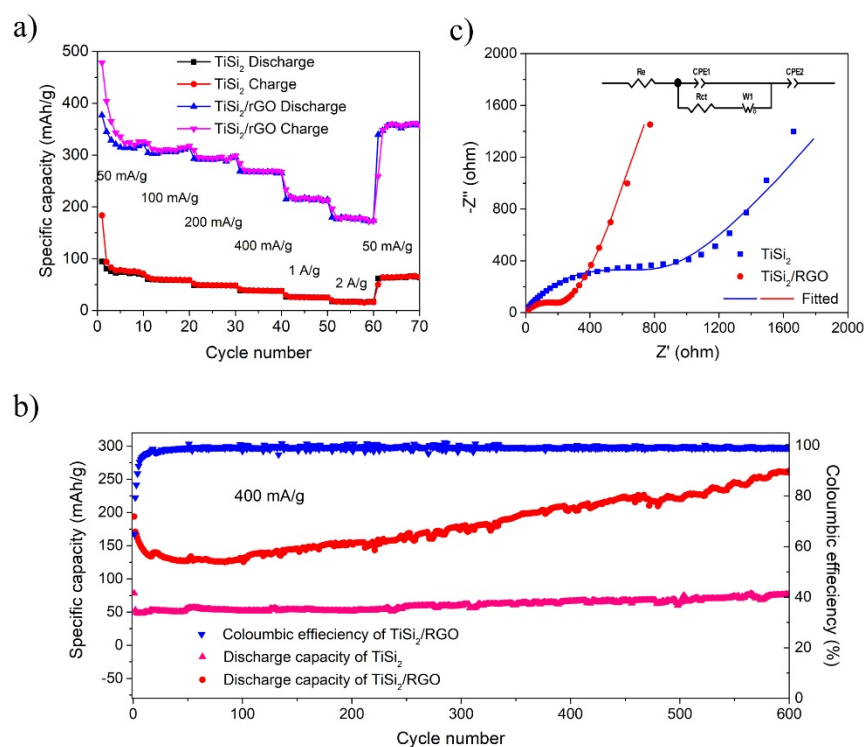
Figure 3. (**a**) rate performance of $TiSi_2$ and $TiSi_2$/RGO; (**b**) cycle performance and coulombic efficiency of $TiSi_2$ and $TiSi_2$/RGO at a current density of 400mA/gt; (**c**) Nyquist plots of $TiSi_2$ and $TiSi_2$/RGO.

In order to further investigate the lithium-ion storage property of these two anodes, electrochemical impedance spectroscopy (EIS) was employed at room temperature. It can be seen from Figure 3c—that both Nyquist plots are mainly composed of two parts: a semicircle in the high-frequency region represents the resistance at the Ohmic surface layer [40], and an oblique line in the low-frequency region indicates an ion diffusion procedure. The Nyquist plots were fitted using the modified Randles equivalent circuit (the inset in Figure 3c). Based on the fitting results, the $TiSi_2$/RGO hybrid material exhibits a lower charge-transfer resistance of 209.6 Ω, while $TiSi_2$ shows a higher transfer resistance of 920.0 Ω, suggesting the reduced graphene oxide improves the electronic conductivity significantly and $TiSi_2$/RGO hybrid obtains a faster charge-transfer process as a result. This result is in a good agreement with the enhancement of electrochemical performance of $TiSi_2$/graphene hybrid.

To confirm the detail of phase transformation during the lithiation/delithiation process, the $TiSi_2$/RGO electrodes have been checked by XRD at different charge/discharge potentials (Figure 4). Compared with XRD pattern of the fresh electrode (Figure 4a), there is a new peak that appeared at ~37° in the XRD pattern when the electrode was charged to 1.2 V (Figure 4b) and 0 V (Figure 4c), indicating the formation of TiSi phase. Then this peak is disappeared when the electrode was discharged to 2.1 V (Figure 4d), which is probably due to the transformation from TiSi to $TiSi_2$. According to the ex situ XRD results and in comparison with the reactions of $MoSi_2$ and $CrSi_2$ during the lithiation/delithiation process [15], $TiSi_2$ would like to follow the reaction shown in Equation (1) [9]:

$$3TiSi_2 + 7Li^+ + 7e^- \longleftrightarrow 3TiSi + 3SiLi_{2.33} \tag{1}$$
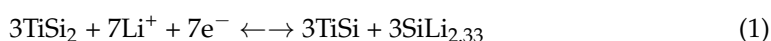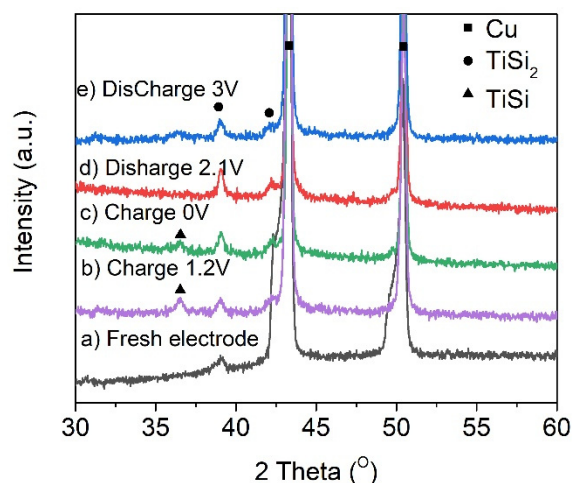
Figure 4. XRD patterns of TiSi$_2$/RGO electrode at different charge/discharge potentials.

This work further demonstrated that the Li-ion storage potential of inactive transition metal silicides is promising, as reported in our earlier work [41]. According to Equation (1), assuming TiSi$_2$ can transform completely to TiSi and SiLi$_{2.33}$, theoretical capacity values of 600 mAh/g can be expected for TiSi$_2$. If TiSi could further decompose to Ti$_5$Si$_3$ or Ti$_3$Si, this would increase the capacities to 840 or 1000 mAh/g, respectively. These capacity values are much higher than the initial reversible capacity of TiSi$_2$ and TiSi$_2$/RGO electrodes obtained in this work. However, with the charge-discharge cycles, a reversible capacity of 263 mAh/g at 400 mA/g was achieved for TiSi$_2$/RGO hybrid, increased by 51% compared to the 2nd charge capacity, suggesting that increasingly more TiSi$_2$ grains are decomposed with cycling. Thus it is rational to predict that the electrochemical performance of TiSi$_2$ can be further remarkably enhanced by decreasing the particle size and engineering the materials' structure and composition. In addition, compared to other inactive transition metal silicides (Table 1), the TiSi$_2$/rGO electrode shows a moderate specific capacity and best capacity retention after cycles. Moreover, if using ionic liquid as electrolyte, this electrode may have a chance to achieve better electrochemical performance [42]. Combination of a relatively high capacity, low volume changes upon cycling and excellent rate capability of TiSi$_2$/RGO hybrid, TiSi$_2$ or other inactive transition metal silicides may become the next anode material to substitute graphite, silicon or lithium titanate, or at least act as high-rate electrode for Li-ion battery and capacitor.

Table 1. Comparison of electrochemical performance of different inactive transition metal silicides.

Materials	Electrolyte	Specific Capacity (mAh/g)	Capacity Retention/Cycles	Ref.
CrSi$_2$	1 M LiFSA/Py13-FSA	240 (50 mA/g)	89%/300	[42]
FeSi$_2$	1 M LiFSA/Py13-FSA	630 (50 mA/g)	85%/300	[42]
FeSi$_2$	1 M LiTFSA/PC	700 (50 mA/g)	15%/300	[42]
NiSi$_2$	1 M LiFSA/Py13-FSA	820 (50 mA/g)	58%/250	[42]
Nano-NiSi$_2$	1 M LiPF$_6$/EC-DC-FEC	313 (87.5 mA/g)	~88%/60	[43]
MoSi$_2$	1 M LiPF$_6$/EC-DMC-EMC	153 (134 mA/g)	127%/100	[41]
MoSi$_2$	1 M LiPF$_6$/EC-DMC	~110 (67 mA/g)	-	[15]
TiSi$_2$/rGO	1 M LiPF$_6$/EC-DMC-EMC	378 (50 mA/g)	136%/600	This work

4. Conclusions

In summary, the electrochemical performance of pure TiSi$_2$ and TiSi$_2$/RGO hybrid as anode materials for LIB was investigated in this work. Pure TiSi$_2$ was obtained by the "chemical oven" self-propagating high-temperature synthesis from the element reactants. TiSi$_2$/RGO hybrid was synthesized through reducing the graphene oxide/TiSi$_2$ suspension

by hydrazine. Benefiting from the high conductivity, the hybrid exhibits better activities than pure $TiSi_2$ in the reversible lithiation and delithiation process, and its reversible specific capacity is ~263 mAh/g after 600 cycles at 400 mA/g, increased by 2.4 times compared to that of pure $TiSi_2$. There are lots of inactive transition metal silicides with low activity at room temperature reported in literature, such as $MoSi_2$, WSi_2, and most of them have potentials such as good conductivity, good stability even under severe environments for using as an anode. Our discoveries are suggesting and encouraging the investigation on the inactive transition metal silicides as valuable electrodes as Li-ion battery and capacitor.

Author Contributions: Conceptualization, J.X. and W.Y.; formal analysis, M.J.; investigation, X.S., Q.L. and C.G.; writing—original draft preparation, J.X.; writing—review and editing, J.X. and W.Y.; supervision, J.X. and W.Y.; project administration, J.X. and W.Y.; funding acquisition, J.X. and W.Y. All authors have read and agreed to the published version of the manuscript.

Data Availability Statement: No new data were created or analyzed in this study. Data sharing is not applicable to this article.

Conflicts of Interest: The authors declare no conflict of interest.

References

1. Kostopoulou, A.; Vernardou, D.; Makri, D.; Brintakis, K.; Savva, K.; Stratakis, E. Highly stable metal halide perovskite micro-cube anodes for lithium-air batteries. *J. Power Sources Adv.* **2020**, *3*, 100015. [CrossRef]
2. Li, P.; Kim, H.; Myung, S.; Sun, Y. Diverting Exploration of Silicon Anode into Practical Way: A Review Focused on Sili-con-Graphite Composite for Lithium Ion Batteries. *Energy Storage Mater.* **2021**, *35*, 550–576. [CrossRef]
3. Wang, J.; Liao, L.; Lee, H.R.; Shi, F.; Huang, W.; Zhao, J.; Pei, A.; Tang, J.; Zheng, X.; Chen, W.; et al. Surface-engineered meso-porous silicon microparticles as high-Coulombic-efficiency anodes for lithium-ion batteries. *Nano Energy* **2019**, *61*, 404–410. [CrossRef]
4. Hui, X.; Zhao, R.; Zhang, P.; Li, C.; Wang, C.; Yin, L. Low-temperature reduction strategy synthesized Si/Ti_3C_2 MXene compo-site anodes for high-performance li-ion batteries. *Adv. Energy Mater.* **2019**, *9*, 1901065. [CrossRef]
5. Sung, J.; Ma, J.; Choi, S.; Hong, J.; Kim, N.; Chae, S.; Son, Y.; Kim, S.Y.; Cho, J. Fabrication of lamellar nanosphere structure for effective Stress-Management in Large-Volume-Variation anodes of High-Energy Lithium-Ion batteries. *Adv. Mater.* **2019**, *31*, 1900970. [CrossRef] [PubMed]
6. Chen, H.; Wu, Z.; Su, Z.; Chen, S.; Yan, C.; Al-Mamun, M.; Tang, Y.; Zhang, S. A mechanically robust self-healing binder for silicon anode in lithium ion batteries. *Nano Energy* **2021**, *81*, 105654. [CrossRef]
7. Liu, S.; Zhang, X.; Yan, P.; Cheng, R.; Tang, Y.; Cui, M.; Wang, B.; Zhang, L.; Wang, X.; Jiang, Y.; et al. Dual bond enhanced multidimensional constructed composite silicon anode for High-Performance lithium ion batteries. *ACS Nano* **2019**, *13*, 8854–8864. [CrossRef] [PubMed]
8. Liu, J.; Li, N.; Goodman, M.D.; Zhang, H.G.; Epstein, E.S.; Huang, B.; Pan, Z.; Kim, J.; Choi, J.H.; Huang, X.; et al. Mechanically and Chemically Robust Sandwich-Structured C@Si@C Nanotube Array Li-Ion Battery Anodes. *ACS Nano* **2015**, *9*, 1985–1994. [CrossRef]
9. Anani, A.; Huggins, R. Multinary alloy electrodes for solid state batteries I. A phase diagram approach for the selection and storage properties determination of candidate electrode materials. *J. Power Sources* **1992**, *38*, 351–362. [CrossRef]
10. Kasavajjula, U.; Wang, C.; Appleby, A.J. Nano- and bulk-silicon-based insertion anodes for lithium-ion secondary cells. *J. Power Sources* **2007**, *163*, 1003–1039. [CrossRef]
11. Ding, B.; Cai, Z.; Ahsan, Z.; Ma, Y.; Zhang, S.; Song, G.; Yuan, C.; Yang, W.; Wen, C. A Review of Metal Silicides for Lithium-Ion Battery Anode Application. *Acta Met. Sin. (English Lett.)* **2021**, *34*, 291–308. [CrossRef]
12. Liu, Y.; He, Y.; Ma, R.; Gao, M.; Pan, H. Improved lithium storage properties of Mg2Si anode material synthesized by hydro-gen-driven chemical reaction. *Electrochem. Commun.* **2012**, *25*, 15–18. [CrossRef]
13. Yan, J.; Huang, H.; Zhang, J.; Yang, Y. The study of Mg_2Si/carbon composites as anode materials for lithium ion batteries. *J. Power Sources* **2008**, *175*, 547–552. [CrossRef]
14. Tamirat, A.G.; Hou, M.; Liu, Y.; Bin, D.; Sun, Y.; Fan, L.; Wang, Y.; Xia, Y. Highly stable carbon coated Mg_2Si intermetallic nano-particles for lithium-ion battery anode. *J. Power Sources* **2018**, *384*, 10–17. [CrossRef]
15. Courtel, F.M.; Duguay, D.; Abu-Lebdeh, Y.; Davidson, I.J. Investigation of $CrSi_2$ and $MoSi_2$ as anode materials for lithium-ion batteries. *J. Power Sources* **2012**, *202*, 269–275. [CrossRef]
16. Netz, A.; Huggins, R.A.; Weppner, W. Investigations of a number of alternative negative electrode materials for use in lithium cells. *Ionics* **2001**, *7*, 433–439. [CrossRef]

17. Zhou, S.; Wang, D. Unique Lithiation and Delithiation Processes of Nanostructured Metal Silicides. *ACS Nano* **2010**, *4*, 7014–7020. [CrossRef]

18. Yeh, C.; Chen, W.; Hsu, C. Formation of titanium silicides Ti_5Si_3 and $TiSi_2$ by self-propagating combustion synthesis. *J. Alloy. Compd.* **2007**, *432*, 90–95. [CrossRef]

19. Yeh, C.; Wang, H.; Chen, W. A comparative study on combustion synthesis of Ti–Si compounds. *J. Alloy. Compd.* **2008**, *450*, 200–207. [CrossRef]

20. Liu, J.; Bai, Y.; Chen, P.; Cui, N.; Yin, H. Reaction synthesis of $TiSi_2$ and Ti_5Si_3 by ball-milling and shock loading and their photocatalytic activities. *J. Alloy. Compd.* **2013**, *555*, 375–380. [CrossRef]

21. Liang, B.; Liu, Y.; Xu, Y. Silicon-based materials as high capacity anodes for next generation lithium ion batteries. *J. Power Sources* **2014**, *267*, 469–490. [CrossRef]

22. Zhou, S.; Liu, X.; Wang, D. $Si/TiSi_2$ Heteronanostructures as High-Capacity Anode Material for Li Ion Batteries. *Nano Lett.* **2010**, *10*, 860–863. [CrossRef] [PubMed]

23. Zhou, S.; Yang, X.; Lin, Y.; Xie, J.; Wang, D. A Nanonet-Enabled Li Ion Battery Cathode Material with High Power Rate, High Capacity, and Long Cycle Lifetime. *ACS Nano* **2012**, *6*, 919–924. [CrossRef] [PubMed]

24. Zhang, H.; Zhong, X.; Shaw, J.C.; Liu, L.; Huang, Y.; Duan, X. Very high energy density silicide–air primary batteries. *Energy Environ. Sci.* **2013**, *6*, 2621. [CrossRef]

25. Zhang, X.; Xie, X.; Wang, H.; Zhang, J.; Pan, B.; Xie, Y. Enhanced Photoresponsive Ultrathin Graphitic-Phase C_3N_4 Nanosheets for Bioimaging. *J. Am. Chem. Soc.* **2013**, *135*, 18–21. [CrossRef]

26. Lindsay, L.; Broido, D.A. Enhanced thermal conductivity and isotope effect in single-layer hexagonal boron nitride. *Phys. Rev. B* **2011**, *84*, 155421. [CrossRef]

27. Chen, S.; Wu, Q.; Mishra, C.; Kang, J.; Zhang, H.; Cho, K.; Cai, W.; Balandin, A.A.; Ruoff, R.S. Thermal conductivity of isotopically modified graphene. *Nat. Mater.* **2012**, *11*, 203–207. [CrossRef]

28. Yoo, E.; Kim, J.; Hosono, E.; Zhou, H.-S.; Kudo, T.; Honma, I. Large Reversible Li Storage of Graphene Nanosheet Families for Use in Rechargeable Lithium Ion Batteries. *Nano Lett.* **2008**, *8*, 2277–2282. [CrossRef]

29. Li, X.; Geng, D.; Zhang, Y.; Meng, X.; Li, R.; Sun, X. Superior cycle stability of nitrogen-doped graphene nanosheets as anodes for lithium ion batteries. *Electrochem. Commun.* **2011**, *13*, 822–825. [CrossRef]

30. Mukherjee, R.; Thomas, A.V.; Krishnamurthy, A.; Koratkar, N. Photothermally Reduced Graphene as High-Power Anodes for Lithium-Ion Batteries. *ACS Nano* **2012**, *6*, 7867–7878. [CrossRef]

31. Zhang, Z.; Wang, Y.; Ren, W.; Tan, Q.; Chen, Y.; Li, H.; Zhong, Z.; Su, F. Scalable synthesis of interconnected porous Silicon/Carbon composites by the rochow reaction as High-Performance anodes of lithium ion batteries. *Angew. Chem.* **2014**, *126*, 5165–5169. [CrossRef]

32. Yi, R.; Zai, J.; Dai, F.; Gordin, M.L.; Wang, D. Dual conductive network-enabled graphene/Si–C composite anode with high areal capacity for lithium-ion batteries. *Nano Energy* **2014**, *6*, 211–218. [CrossRef]

33. Xu, J.; Zhang, H.; Yan, J.; Zhang, B.; Li, W. Effect of argon atmosphere on the formation of $MoSi_2$ by self-propagating combus-tion method. *Int. J. Refract. Metals Hard Mater.* **2007**, *25*, 318–321. [CrossRef]

34. Chen, F.; Xu, J.; Yan, J.; Tang, S. Effects of Y_2O_3 on $SiC/MoSi_2$ composite by mechanical-assistant combustion synthesis. *Int. J. Refract. Met. Hard Mater.* **2013**, *36*, 143–148. [CrossRef]

35. Trambukis, J.; Munir, Z.A. Effect of Particle Dispersion on the Mechanism of Combustion Synthesis of Titanium Silicide. *J. Am. Ceram. Soc.* **1990**, *73*, 1240–1245. [CrossRef]

36. Marcano, D.C.; Kosynkin, D.V.; Berlin, J.M.; Sinitskii, A.; Sun, Z.; Slesarev, A.; Alemany, L.B.; Lu, W.; Tour, J.M. Improved syn-thesis of graphene oxide. *ACS Nano* **2010**, *4*, 4806–4814. [CrossRef] [PubMed]

37. Ahn, W.; Kang, K.; Kim, K. Synthesis of TS-1 by microwave heating of template-impregnated SiO_2–TiO_2 xerogels. *Catal. Lett.* **2001**, *72*, 229–232. [CrossRef]

38. Han, Y.; Liu, X.; Lu, Z. Systematic Investigation of Prelithiated SiO_2 Particles for High-Performance Anodes in Lithium-Ion Battery. *Appl. Sci.* **2018**, *8*, 1245. [CrossRef]

39. Wu, H.; Zheng, G.; Liu, N.; Carney, T.J.; Yang, Y.; Cui, Y. Engineering Empty Space between Si Nanoparticles for Lithium-Ion Battery Anodes. *Nano Lett.* **2012**, *12*, 904–909. [CrossRef] [PubMed]

40. Lin, D.; Lu, Z.; Hsu, P.-C.; Lee, H.R.; Liu, N.; Zhao, J.; Wang, H.; Liu, C.; Cui, Y. A high tap density secondary silicon particle anode fabricated by scalable mechanical pressing for lithium-ion batteries. *Energy Environ. Sci.* **2015**, *8*, 2371–2376. [CrossRef]

41. Xu, J.; Zhang, Y.; Qi, J.; Wang, Y.; Luo, J.; Yao, W. Preparation of nanocrystalline $MoSi_2$ with enhanced lithium storage by sol–gel and carbonthermal reduction method. *Ceram. Int.* **2018**, *44*, 9494–9498. [CrossRef]

42. Domi, Y.; Usui, H.; Takaishi, R.; Sakaguchi, H. Lithiation and Delithiation Reactions of Binary Silicide Electrodes in an Ionic Liquid Electrolyte as Novel Anodes for Lithium-Ion Batteries. *ChemElectroChem* **2018**, *6*, 581–589. [CrossRef]

43. Du, Z.; Hatchard, T.D.; Bissonnette, P.; Dunlap, R.A.; Obrovac, M.N. Electrochemical activity of nano-$NiSi_2$ in Li Cells. *J. Elec-trochem. Soc.* **2016**, *163*, A2456–A2460. [CrossRef]